Available online at www.sciencedirect.com
ScienceDirect
Trans. Nonferrous Met. Soc. China 29(2019) 722−734
Transactions of Nonferrous Metals Society of China
www.tnmsc.cn

Effect of Zn addition on microstructure and mechanical properties of cast Mg−Gd−Y−Zr alloys

Zhi-bing DING[1,2], Yu-hong ZHAO[1], Ruo-peng LU[1], Mei-ni YUAN[2], Zhi-jun WANG[2], Hui-jun LI[3], Hua HOU[1]

1. College of Materials Science and Engineering, North University of China, Taiyuan 030051, China;
2. College of Mechatronic Engineering, North University of China, Taiyuan 030051, China;
3. School of Mechanical, Materials and Mechatronic Engineering, University of Wollongong, Wollongong, NSW 2522, Australia

Received 5 May 2018; accepted 23 July 2018

Abstract: The effects of Zn addition on the microstructure and mechanical properties of Mg−10Gd−3Y−0.6Zr (wt.%) alloys in the as-cast, solution-treated, and peak-aged conditions were investigated. Experimental results reveal that the microstructure of the as-cast alloy without Zn consists of α-Mg and $Mg_{24}(Gd,Y)_5$ phases, and the alloy with 0.5 wt.% Zn consists of α-Mg, $(Mg,Zn)_3(Gd,Y)$ and $Mg_{24}(Gd,Y,Zn)_5$ phases. With the addition of Zn increasing to 1 wt.%, the $Mg_{24}(Gd,Y,Zn)_5$ phase disappears and some needle-like stacking faults distribute along the grain boundaries. Moreover, the 18R long-period stacking ordered (LPSO) phase is observed in the as-cast alloy with 2 wt.% Zn. After solution treatment, the $Mg_{24}(Gd,Y)_5$ and $Mg_{24}(Gd,Y,Zn)_5$ eutectic phases are completely dissolved, and the $(Mg,Zn)_3(Gd,Y)$ phase, needle-like stacking faults and 18R LPSO phase all transform into 14H LPSO phase. Both the suitable volume fraction of 14H LPSO phases and the fine ellipsoidal-shaped β' phases make the peak-aged alloy with 0.5 wt.% Zn exhibit excellent comprehensive mechanical properties and the UTS, YS and elongation are 338 MPa, 201 MPa and 6.8%, respectively.

Key words: Mg alloy; heat treatment; microstructure; mechanical property; LPSO phase

1 Introduction

Light weight magnesium (Mg) alloys are of great potential to be used in the aerospace, biomedical devices and automotive industries for their low densities, good damping capacity, distinct strength, and excellent machinability [1−5]. However, the poor mechanical properties, such as low yield and tensile strength have restricted their extensive applications. Recently, Mg alloys containing rare-earth (RE) elements have received much attention. In all of the Mg−RE alloys, the most prominent alloys are Mg−Gd−Y−Zn series. The Mg−Gd−Y−Zn series alloys usually possess excellent mechanical properties at both ambient and elevated temperatures due to the combined effects of the formation of the long-period stacking ordered (LPSO) and β' phases during heat treatment. In Mg−8.2Gd−3.8Y−1.0Zn−0.4Zr (wt.%) alloy, high ultimate tensile strength (UTS) of about 517 MPa, yield strength (YS) of 426 MPa and elongation of 4.5% were obtained by hot rolling and aging [6]. WANG et al [7] developed a high-strength Mg−8.40Gd−5.30Y−1.65Zn−0.59Mn (wt.%) alloy with UTS of 500 MPa, YS of 322 MPa and elongation of 10.0% after hot extrusion and aging.

The LPSO phase was first reported in Mg−Zn−Zr−Y alloy, called *X* phase by LUO and ZHANG [8]. The Mg−RE−Zn alloys with RE/Zn molar ratio in the range of 1−3 can form LPSO phases in the process of casting or annealing [9−11]. Different authors have proposed different types of LPSO structures in the Mg−RE−Zn series alloys, including 6H, 10H, 14H, 18R and 24R [12−14]. It is widely known that the mechanical properties of the Mg−RE−Zn alloys can be improved significantly by the LPSO phases. KAWAMURA et al [15] fabricated a $Mg_{97}Zn_1Y_2$ (at.%) alloy, which exhibited superior mechanical properties with UTS of about 610 MPa and elongation of 5%, by rapidly

Foundation item: Projects (51774254, 51774253, 51701187, U1610123, 51674226, 51574207, 51574206) supported by the National Natural Science Foundation of China; Project (MC2016-06) supported by the Science and Technology Major Project of Shanxi Province, China; Project (201601D021062) supported by Shanxi Province Science Foundation for Youths, China
Corresponding author: Yu-hong ZHAO; Tel: +86-351-3557006; Fax: +86-351-3557118; E-mail: zhaoyuhong@nuc.edu.cn
DOI: 10.1016/S1003-6326(19)64982-4

solidified powder metallurgy.

While some alloys can achieve high strength, they cannot simultaneously exhibit high strength and good ductility. Accordingly, balancing the strength and ductility of cast Mg alloy is a critical concern for engineering applications. The proper control of the morphology, size, volume fraction and distribution of the reinforced phase is of great significance to the optimization of the mechanical properties of the alloys. Alloying is a relatively simple and effective method. In the present work, Mg−10Gd−3Y−*x*Zn−0.6Zr (*x*=0, 0.5, 1 and 2, wt.%) alloys were produced using the method of water-cooled steel crucible casting ingot processing. The evolution of microstructure and mechanical properties from the as-cast to the solution-treated and aging-treated conditions were systematically examined. The effects of Zn element on the formation of the stacking faults and LPSO phases, age hardening behaviors and mechanical properties were investigated. The effects of the LPSO and *β′* phases coexisting together on the mechanical properties of Mg−Gd−Y−Zn−Zr alloys were discussed.

2 Experimental

The alloy ingots with nominal compositions of Mg−10Gd−3Y−*x*Zn−0.6Zr (*x*=0, 0.5, 1 and 2, wt.%, indentified as A, B, C and D, respectively) were melted from pure Mg and Zn, Mg−30%Gd, Mg−30%Y and Mg−30%Zr master alloys. Melting was conducted in an medium frequency induction heating furnace using a small steel crucible with a diameter of 98 mm under the protection of Ar atmosphere at 780 °C. The melt was cooled in water after adequate stirring. The ingots were solution-treated at 520 °C for 8 h followed by an immediate water quenching. Artificial ageing process was carried out at 220 °C in order to investigate the age hardening behaviors with different ageing time.

The chemical compositions of the alloys were determined by inductively coupled plasma spectroscopy and are listed in Table 1. The microstructures of the as-cast and solution-treated specimens were observed by using an optical microscope (OM). Phase analysis were conducted using a Rigaku D/MAX2500PC X-ray diffractometer with a copper target at scanning angles from 20° to 90° and scanning speed of 5 (°)/min. The morphology and elemental composition of the specimens were determined by using scanning electron microscopy (SEM, SU5000) equipped with an energy dispersive spectroscopy (EDS). The detailed microstructures of the samples were further analyzed using a transmission electron microscope (TEM, JEM−2100F) operated at an accelerating voltage of 200 kV. The average grain size and the volume fraction of second phases were measured by analyzing the optical micrographs with the Image Pro Plus software. At least 300 grains were counted for each alloy.

Table 1 Chemical compositions of cast Mg−Gd−Y−Zn−Zr alloys (wt.%)

Alloy	Nominal composition	Chemical composition				
		Mg	Gd	Y	Zn	Zr
A	Mg−10Gd−3Y−0.6Zr	Bal.	10.03	3.04	0	0.63
B	Mg−10Gd−3Y−0.5Zn−0.6Zr	Bal.	10.10	2.98	0.53	0.61
C	Mg−10Gd−3Y−1Zn−0.6Zr	Bal.	10.05	3.05	0.98	0.59
D	Mg−10Gd−3Y−2Zn−0.6Zr	Bal.	10.13	3.12	2.03	0.60

Tensile tests of above mentioned alloys were performed at a crosshead speed of 1.5 mm/min, according to the relevant standard of using cylindrical specimen with marked dimension of 25 mm in gauge length and 5 mm in diameter. All tensile tests were carried out on a Zwick/Roell Z020 tensile testing machine. An average of three measurements was used. The fracture surfaces were analyzed by SEM.

3 Results

3.1 Microstructures of as-cast alloys

Figure 1 shows the microstructures of the as-cast alloys using OM and SEM, respectively. The microstructure of the as-cast alloys consists of equiaxed *α*-Mg and amounts of eutectics distributing along the grain boundaries discontinuously, as shown in Figs. 1(a), (c), (e) and (g). The higher magnification microstructures of the as-cast alloys obtained by SEM are shown in Figs. 1(b), (d), (f) and (h). With increasing content of Zn, the grain size decreases and the volume fraction of the eutectic phases increases. In as-cast alloys A (Fig. 1(b)) and B (Fig. 1(d)), the bright gray eutectic compounds distribute in grain boundaries in the form of island shape. However, in as-cast alloys C (Fig. 1(f)) and D (Fig. 1(h)), the most of the eutectic phases mainly distribute along the grain boundaries with a hollow-out skeleton morphology.

Figure 2 shows the XRD patterns of the as-cast alloys. It is observed that the alloy A is mainly composed of *α*-Mg and $Mg_{24}(Gd,Y)_5$ phase. However, in the alloy B, the microstructure is mainly composed of *α*-Mg, $Mg_{24}(Gd,Y,Zn)_5$ and $(Mg,Zn)_3(Gd,Y)$ phases. In addition, the $Mg_{12}(Gd,Y)Zn$ phase (LPSO phase) in the alloys C and D notably appear and the $Mg_{24}(Gd,Y,Zn)_5$ phase completely disappeared. The intensity of the diffraction peaks for $(Mg,Zn)_3(Gd,Y)$ and $Mg_{12}(Gd,Y)Zn$ phases are strengthened with increasing the amount of Zn addition.

Figure 3 shows the magnified SEM images of the secondary phase in the as-cast alloys, and the corresponding EDS results are summarized in Table 2. Combined with the XRD results, it is inferred that the

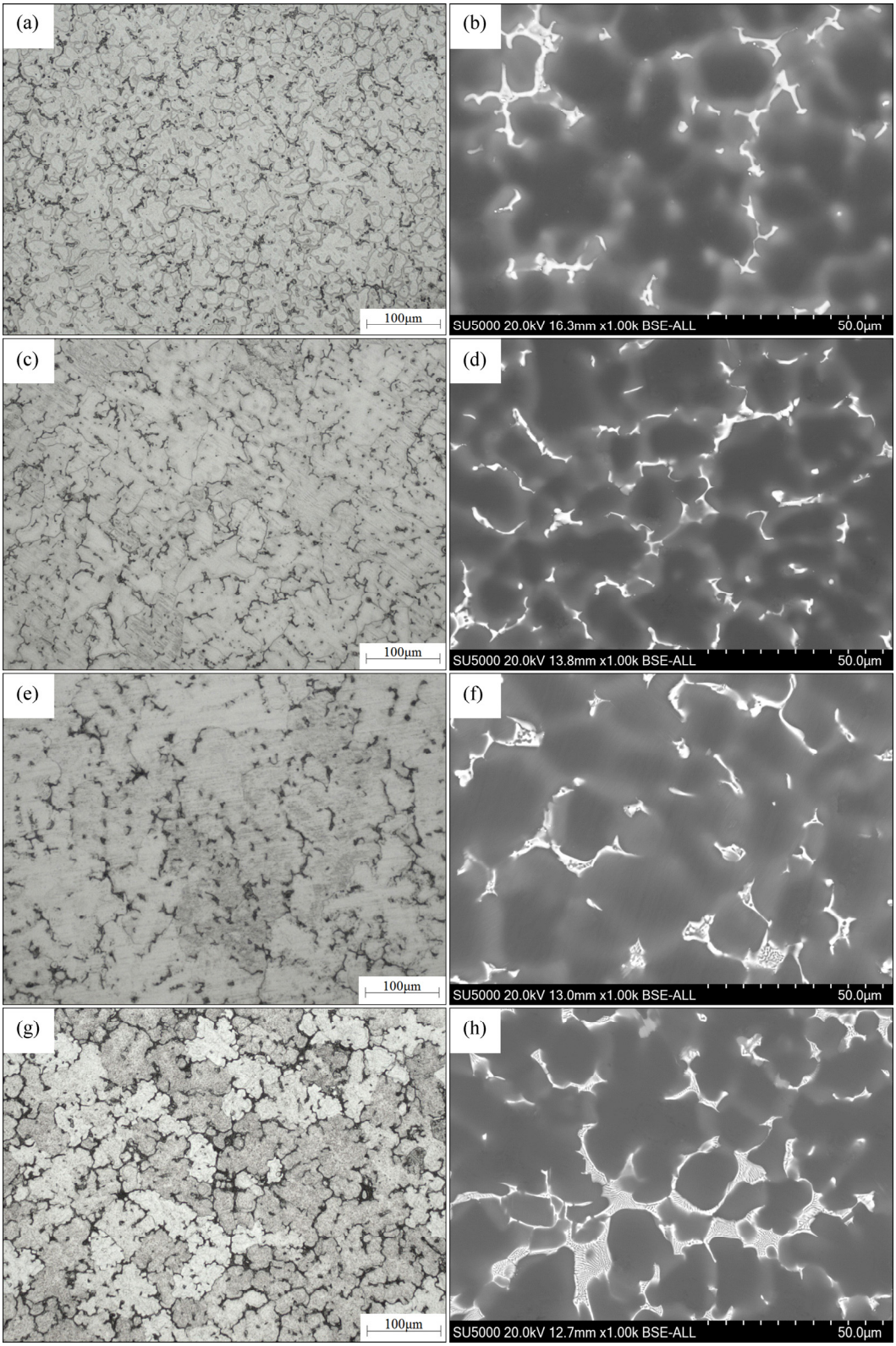

Fig. 1 Optical (a, c, e, g) and SEM (b, d, f, h) images of as-cast alloys: (a, b) Alloy A; (c, d) Alloy B; (e, f) Alloy C; (g, h) Alloy D

island-shaped phases in alloys A and B are mainly composed of $Mg_{24}(Gd,Y)_5$ and $Mg_{24}(Gd,Y,Zn)_5$ phase, respectively. The hollow-out skeleton phase (marked by arrows *C* and *E* in Fig. 3), which was mainly found in alloys C and D, consists of $(Mg,Zn)_3(Gd,Y)$ phases. The volume fraction of the $(Mg,Zn)_3(Gd,Y)$ phase distributing along the grain boundaries increased gradually with increasing Zn content. In addition, some

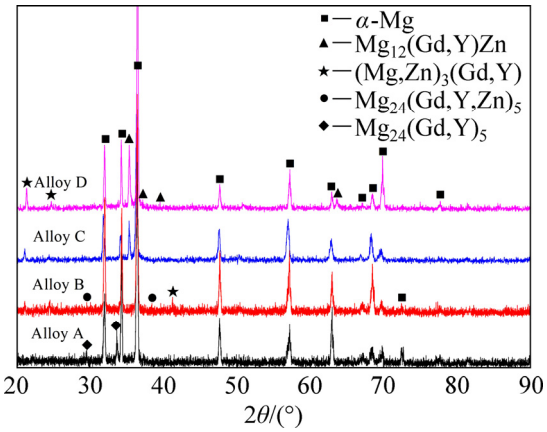

Fig. 2 XRD patterns of as-cast alloys A, B, C and D

needle-like phases can be observed along with the hollow-out skeleton phase in the alloy C. Furthermore, some gray block-shaped phases (marked by arrow *D* in Fig. 3(d)) are observed in the alloy D, attached to the bright phases. The gray block-shaped phase has a composition with RE/Zn ratio of about 1, and mainly consists of $Mg_{12}(Gd,Y)Zn$ phase (LPSO phase).

Figures 4(a) and (b) show the bright-field TEM image and SAED pattern ($B//[11\bar{2}0]_{\alpha}$) of the needle-like phase in as-cast alloy C and the LPSO phase in as-cast alloy D. The needle-like phases (Fig. 4(a)) with a width of several nanometers are parallel to each other. The light streaks appeared between diffraction spots of α-Mg in SAED patterns, demonstrating that these line contrasts are stacking faults on $(0001)_{\alpha}$ basal planes, which is consistent with reports that the simultaneous additions of Y and Zn elements could decrease the stacking fault energy of α-Mg phase on basal plane [16,17]. The LPSO phase (Fig. 4(b)) in as-cast alloy D consists of numerous parallel fine stripes. It is obvious from the corresponding SAED patterns that five extra diffraction spots occur at the intervals between $(0000)_{18R}$ and $(0018)_{18R}$ spots, which further demonstrates that the 18R LPSO phase (a=0.325 nm and c=3.694 nm) [18,19] exists in the as-cast alloy D.

3.2 Microstructures of solution-treated alloys

Figure 5 shows the optical and SEM images of the solution-treated alloys. Compared with as-cast alloys, the grain size increased and the volume fraction of the eutectic compounds decreased after solution treatment, especially alloys A and B. Figure 6 shows the grain size of as-cast and solution-treated alloys. It can be seen that the increment of grain size between the as-cast and the solution-treated alloys decreases with the increase of Zn content, while further increasing the Zn content to 2 wt.%, the solution treatment has a negligible influence on grain size. As shown in Figs. 5(a) and (b), only some cuboid-shaped phases and grain boundaries can be observed, indicating that the eutectic compounds in

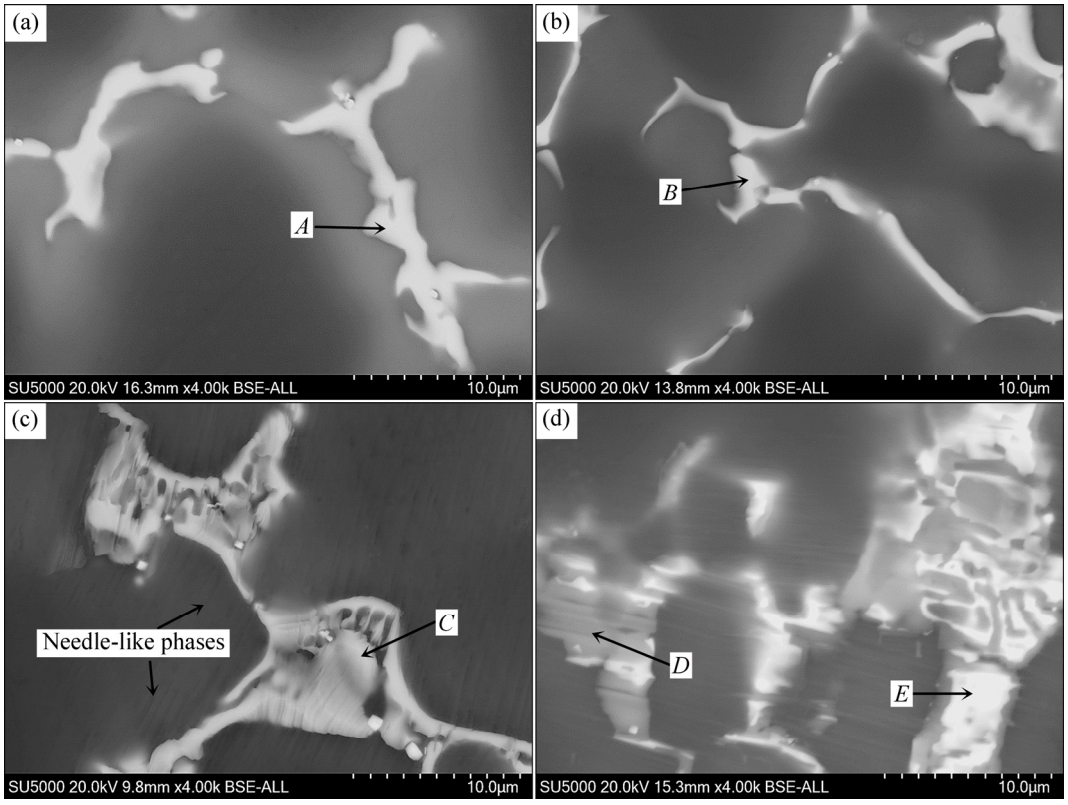

Fig. 3 Magnified SEM images of secondary phase in as-cast alloys: (a) Alloy A; (b) Alloy B; (c) Alloy C; (d) Alloy D

Table 2 EDS elemental analysis results of phases in as-cast alloys in Fig. 3

Point in Fig. 3	wt.%				at.%			
	Mg	Gd	Y	Zn	Mg	Gd	Y	Zn
A	65.29	28.90	5.81	−	91.51	6.26	2.23	−
B	61.99	27.84	5.76	4.41	89.18	6.19	2.26	2.36
C	57.21	29.24	5.82	7.73	86.42	6.83	2.41	4.34
D	68.82	17.60	5.39	8.19	90.48	3.58	1.94	4.00
E	52.24	32.78	6.45	8.53	83.93	8.14	2.83	5.10

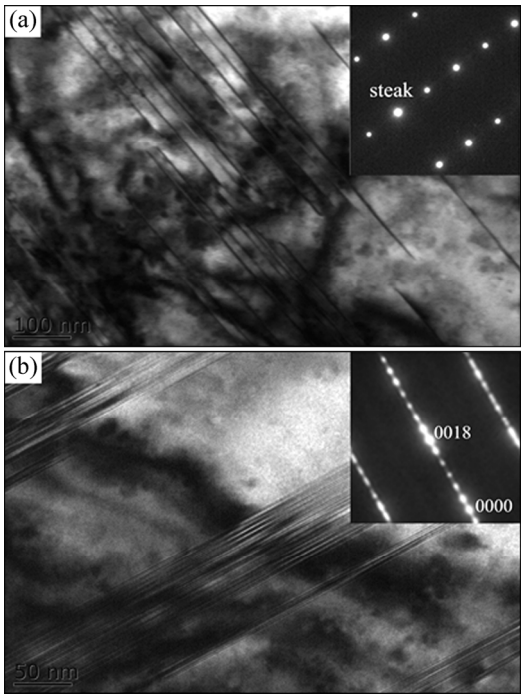

Fig. 4 Bright-field TEM image and corresponding SAED pattern ($B//[11\bar{2}0]_\alpha$) of needle-like phase in as-cast alloy C (a) and LPSO phase in as-cast alloy D (b)

as-cast alloy A have been fully dissolved. Combined with XRD patterns of the solution-treated alloys given in Fig. 7, the dissolution of the $Mg_{24}(Gd,Y)_5$ phase is further confirmed. However, in the other three alloys, some gray phases are observed to distribute along the grain boundaries. Interestingly, several lamellar phases possessing different orientations in different grains are found to grow parallel with one another from the grain boundaries to the grain interior in the solution-treated alloy C, as shown in Figs. 5(e) and (f). XRD patterns of the solution-treated alloys exhibited peaks corresponding to only α-Mg and $Mg_{12}(Gd,Y)Zn$ (LPSO phase), without any other eutectic phase. Therefore, the volume fraction of LPSO phases in the solution-treated alloys detected by Image Pro Plus software is shown in Fig. 8. It is observed that the volume fraction of the LPSO phases increases with increasing content of Zn from 0% to 3.4%, 16.5% and 31.9%. Moreover, it is observed from Fig. 5 that the number density of the cuboid-shaped phases decreases with increasing Zn content. The cuboid-shaped phases with size of 0.8−4 μm mainly distribute at the grain boundary. Combined with the EDS results given in Table 3, the cuboid-shaped phases can be identified as a compound with high contents of the Gd and Y elements. Suitable quantities of cuboid-shaped phases can improve the strength of the alloy, but excessive amounts will lead to the stress concentration near the grain boundary and reduce the mechanical properties [20]. In addition, EDS results of the points *B* and *C* show that the bulk-shaped and lamellar-shaped LPSO phases have an average composition of Mg−3.28Gd−1.93Y−5.25Zn and Mg−3.87Gd−2.31Y−4.57Zn (at.%), respectively.

Figure 9 shows the bright-field TEM image and the corresponding SAED pattern ($B//[11\bar{2}0]_\alpha$) of LPSO phases in the solution-treated alloy C. The corresponding SAED pattern indicates extra weaker spots located at the positions of $n/14$ (where n is an integer) of (0002) α-Mg diffraction. This implies that the LPSO phases are 14H LPSO phases. It can be concluded that the $Mg_{24}(Gd,Y,Zn)_5$, $(Mg,Zn)_3(Gd,Y)$, stacking faults and 18R LPSO phases in as-cast alloys completely transformed into the 14H LPSO phases after solution treatment.

3.3 Aging behaviors of solution-treated alloys and microstructures of peak-aged alloys

Figure 10 shows the age hardening behaviors of the solution-treated alloys at 220 °C, and the standard deviation is given in parenthesis following the value of peak hardness. The solution-treated alloys A, B and C exhibit an obvious age hardening response, while the alloy D displays little ageing hardening behavior. The value of the hardness of the solution-treated alloy A is HV 82, and the hardness increases obviously in 0−10 h, and then reaches a peak hardness of HV 124 after 16 h. It is found that the solution-treated alloy B exhibits an obvious hardening response in 0−20 h, with a best peak hardness of HV 127 obtained at 36 h. The peak hardness of the solution-treated alloy C is obtained after 58 h, with a value of HV 115. However, the solution- treated alloy D does not have an obvious increase in hardness because it contains a large amount of Zn element. The value of the hardness of the solution-treated alloy D is HV 85, and then peak hardness is obtained after 123 h, with a value of HV 91.

The optical microstructures of peak-aged alloys are similar to those of solution-treated alloys and the grain size does not change during ageing treatment. Figure 11 shows the bright-field TEM image and corresponding SAED pattern of the peak-aged alloys. The SAED pattern of the $[2\bar{1}\bar{1}0]_\alpha$ zone axis shows that the extra diffraction spots locate at $1/4(\bar{1}0\bar{1}0)_\alpha$, $1/2(\bar{1}0\bar{1}0)_\alpha$ and $3/4(\bar{1}0\bar{1}0)_\alpha$. Such a diffraction feature indicates

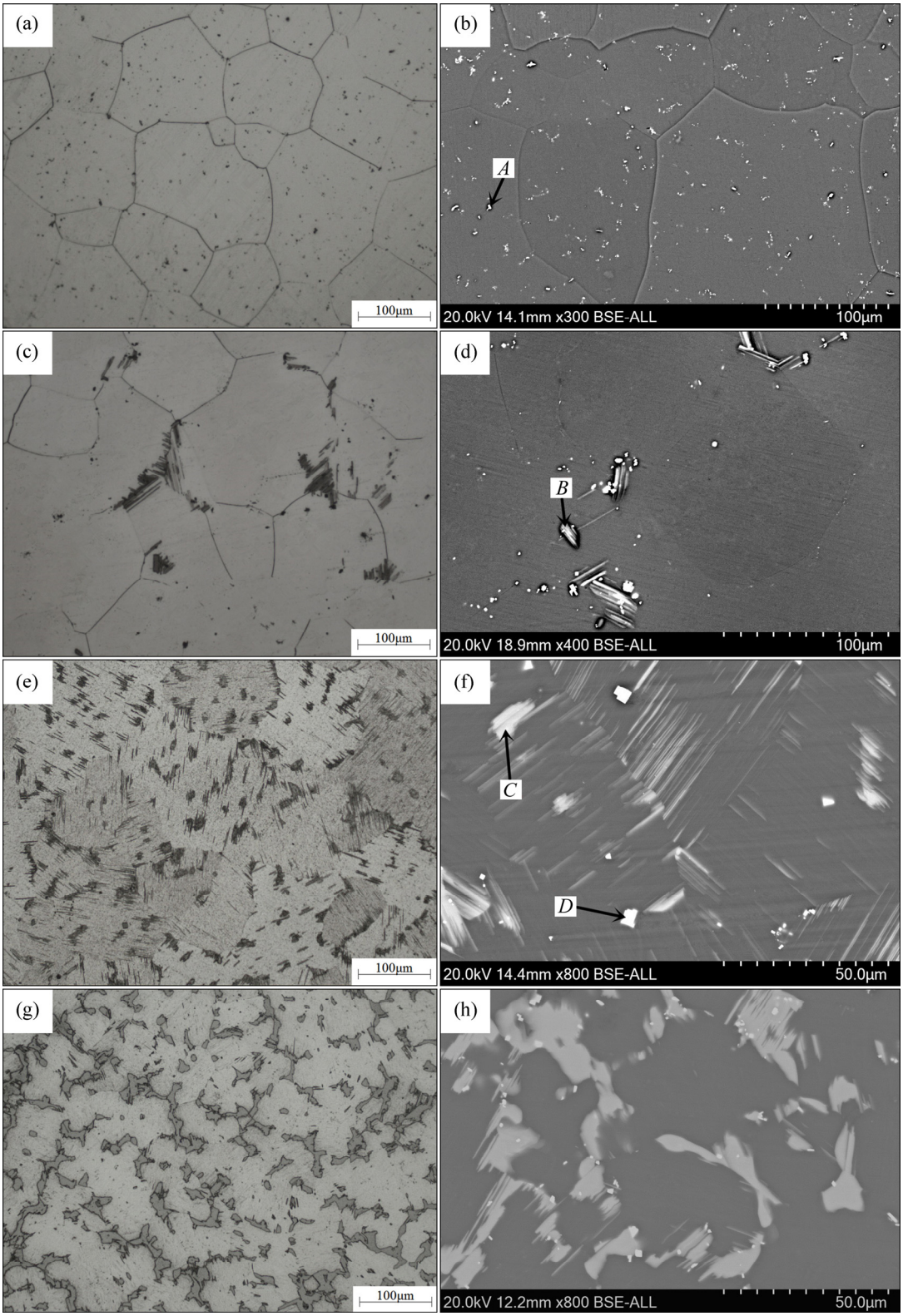

Fig. 5 Optical (a, c, e, g) and SEM (b, d, f, h) images of solution-treated alloys: (a, b) Alloy A; (c, d) Alloy B; (e, f) Alloy C; (g, h) Alloy D

that the ellipsoidal shaped precipitates are β' phases with a bco structure, and the crystal parameters of this phase are: a=0.64 nm, b=2.22 nm and c=0.52 nm, which is consistent with reports [21,22]. The density of ellipsoidal shaped β' phases decreases obviously with increasing Zn content. The average sizes of β' phases in peak-aged alloys A, B, C and D are about 9, 12, 43 and 78 nm in thickness, and 45, 64, 184 and 207 nm in diameter, respectively. It is suggested that the average sizes of this phase increase with increasing Zn content.

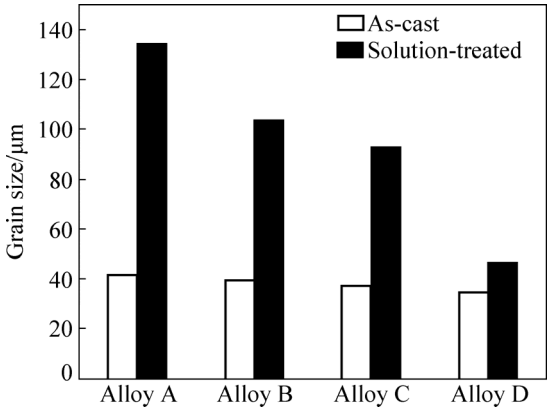

Fig. 6 Grain size of as-cast and solution-treated alloys

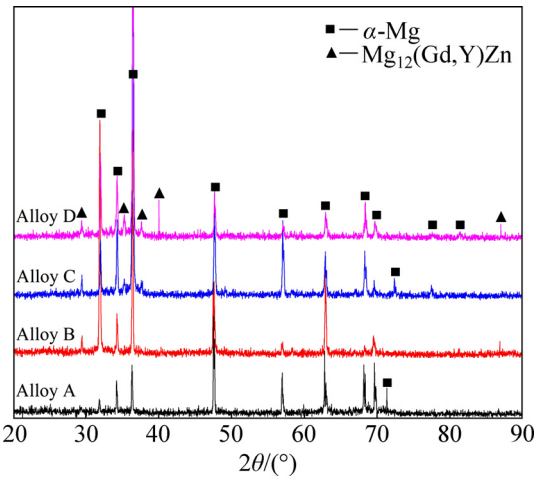

Fig. 7 XRD patterns of solution-treated alloys A, B, C and D

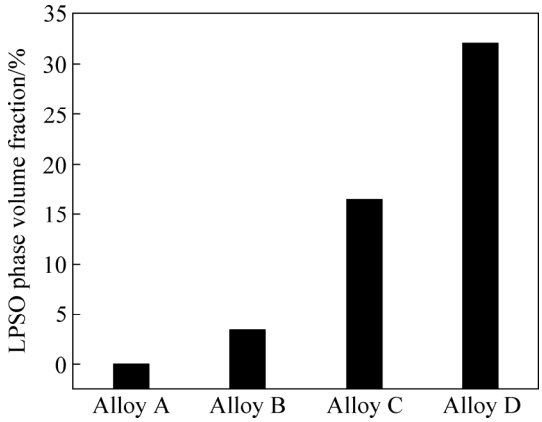

Fig. 8 Volume fraction of LPSO phase in solution-treated alloys

Table 3 EDS elemental analysis results of cuboid-shaped phases and LPSO phases in solution-treated alloys in Fig. 5

Point in Fig. 5	wt.%				at.%			
	Mg	Gd	Y	Zn	Mg	Gd	Y	Zn
A	49.72	30.83	19.44	–	83.14	7.97	8.89	–
B	67.86	16.08	5.36	10.70	89.53	3.28	1.93	5.25
C	66.46	18.62	5.79	9.13	89.42	3.87	2.13	4.57
D	45.15	28.36	25.92	0.57	79.44	7.71	12.47	0.37

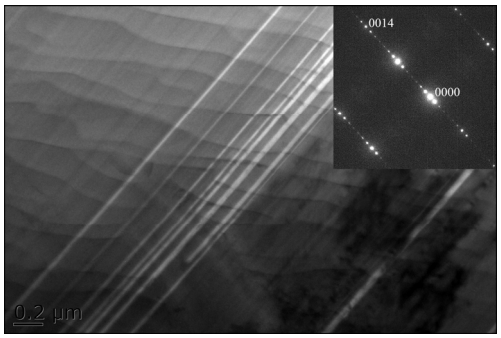

Fig. 9 Bright-field TEM image and corresponding SAED pattern ($B//[11\bar{2}0]_{\alpha}$) of LPSO phase in solution-treated alloy C

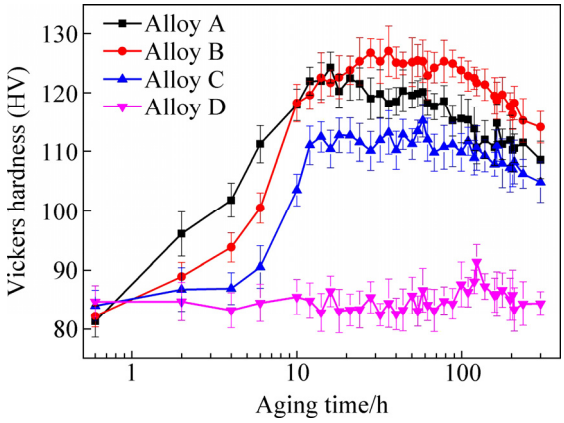

Fig. 10 Age hardening behavior of solution-treated alloys A, B, C and D during aging at 220 °C

Figure 12 shows the bright-field TEM image and corresponding SAED pattern ($B//[11\bar{2}0]_{\alpha}$) of LPSO phase accompanied by β' precipitates in peak-aged alloy C. The 14H LPSO phases do not change during aging treatment. The β' precipitates extend perpendicularly to the 14H LPSO phases. Both the 14H LPSO phases and the fine ellipsoidal shaped β' phases endow the peak-aged Mg−Gd−Y−Zn−Zr alloys with good mechanical properties.

3.4 Mechanical properties

A comparison with typical mechanical properties of the four alloys in different conditions is presented in Fig. 13. The as-cast alloy B shows better mechanical properties than other three as-cast alloys, and the values of the UTS, YS and elongation are 224 MPa, 142 MPa and 5.1%, respectively. The mechanical properties of these alloys are improved after solution treatment, especially elongation. The solution-treated alloy C shows the optimal mechanical properties, and the values of UTS and YS are about 253 MPa and 168 MPa, respectively, with a good elongation of 18.2%. Compared with the as-cast alloy C, the UTS is improved by 37 MPa, and the increment of elongation is up to 13.6%. The tensile strengths of the solution-treated alloys A, B and C are

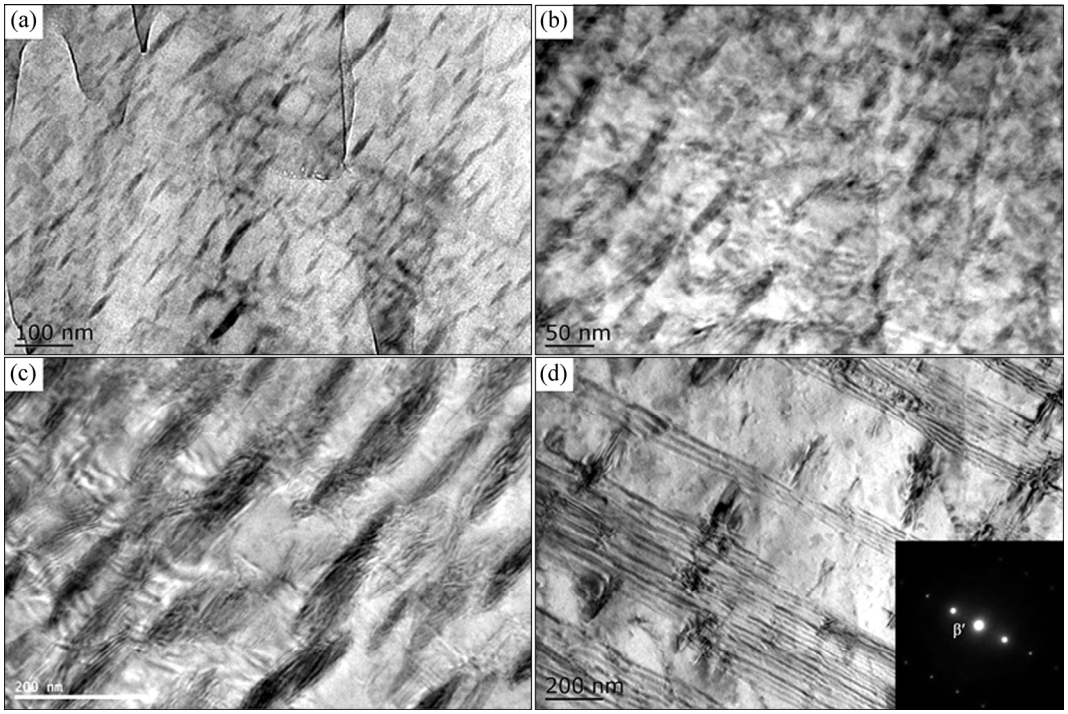

Fig. 11 Bright-field TEM images and corresponding SAED pattern ($B//[2\bar{1}\bar{1}0]_{\alpha}$) of β' precipitates in peak-aged alloys: (a) Alloy A; (b) Alloy B; (c) Alloy C; (d) Alloy D

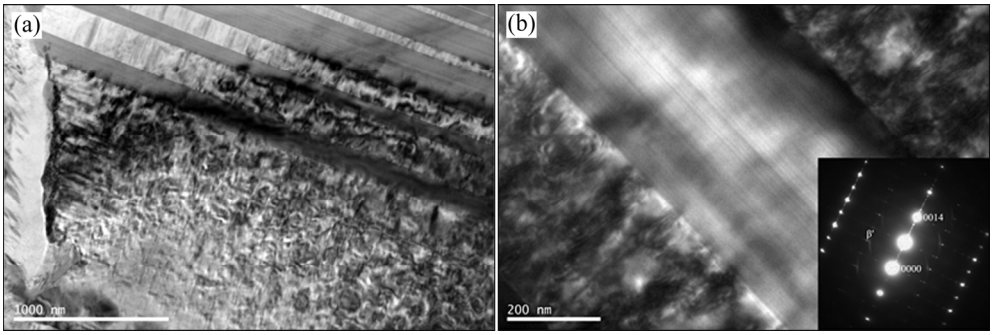

Fig. 12 Bright-field TEM images and corresponding SAED pattern ($B//[11\bar{2}0]_{\alpha}$) of LPSO phase accompanied by β' precipitates in peak-aged alloy C

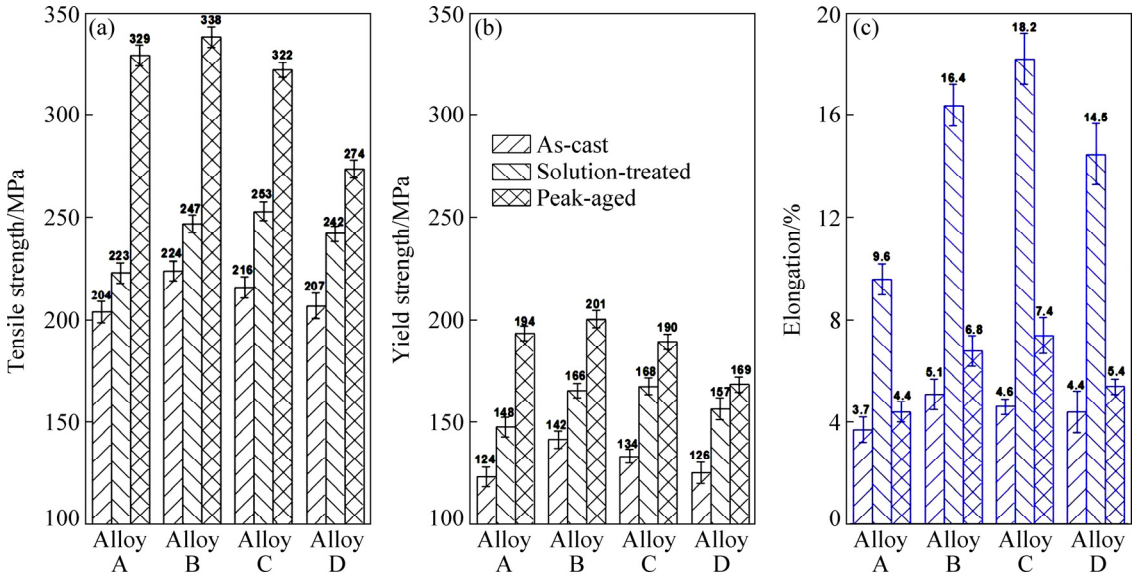

Fig. 13 Mechanical properties of as-cast, solution-treated and peak-aged alloys: (a) Ultimate tensile strength; (b) Yield strength; (c) Elongation

greatly improved after peak aging treatment. Both UTS and YS of peak-aged alloy A are improved significantly, with values of 329 and 194 MPa, respectively. The peak-aged alloy B has the highest mechanical properties, with UTS and YS reaching 338 MPa and 201 MPa, respectively, and an elongation of 6.8%. However, the alloy D with high Zn content has less age hardening response, and the values of the UTS, YS and elongation are 274 MPa, 169 MPa and 5.4%, respectively.

Figure 14 shows the SEM micrographs of the fracture surfaces of as-cast, solution-treated and peak-aged alloys A, B, C and D. The fracture surfaces of as-cast alloys A, C and D show large cleavage planes, tear ridges and few dimples, exhibiting typical brittle fracture. Similar morphology of fracture surfaces is observed in the solution-treated alloy D and peak-aged alloys A and D. A large number of plastic dimples and tear ridges are observed in the fracture surfaces of as-cast alloy B and solution-treated alloys A, B and C, showing typical ductile fracture, which denotes that they have relatively good ductility, in accordance with the tensile results. In addition, some secondary cracks can be observed in the peak-aged alloys B, C and D, which indicates that the precipitation of the ellipsoidal shaped β' phases in the peak-aged alloys can lead to remarkable decrease of tensile ductility. Moreover, tensile fracture surface of the peak-aged alloy B is shown in Fig. 15, which indicates that some cracked particles are cuboid-shaped phases with high content of the RE elements. This suggests that the cuboid-shaped phases can cause stress concentration and act as nucleation sites for the crack initiation during the tensile deformation.

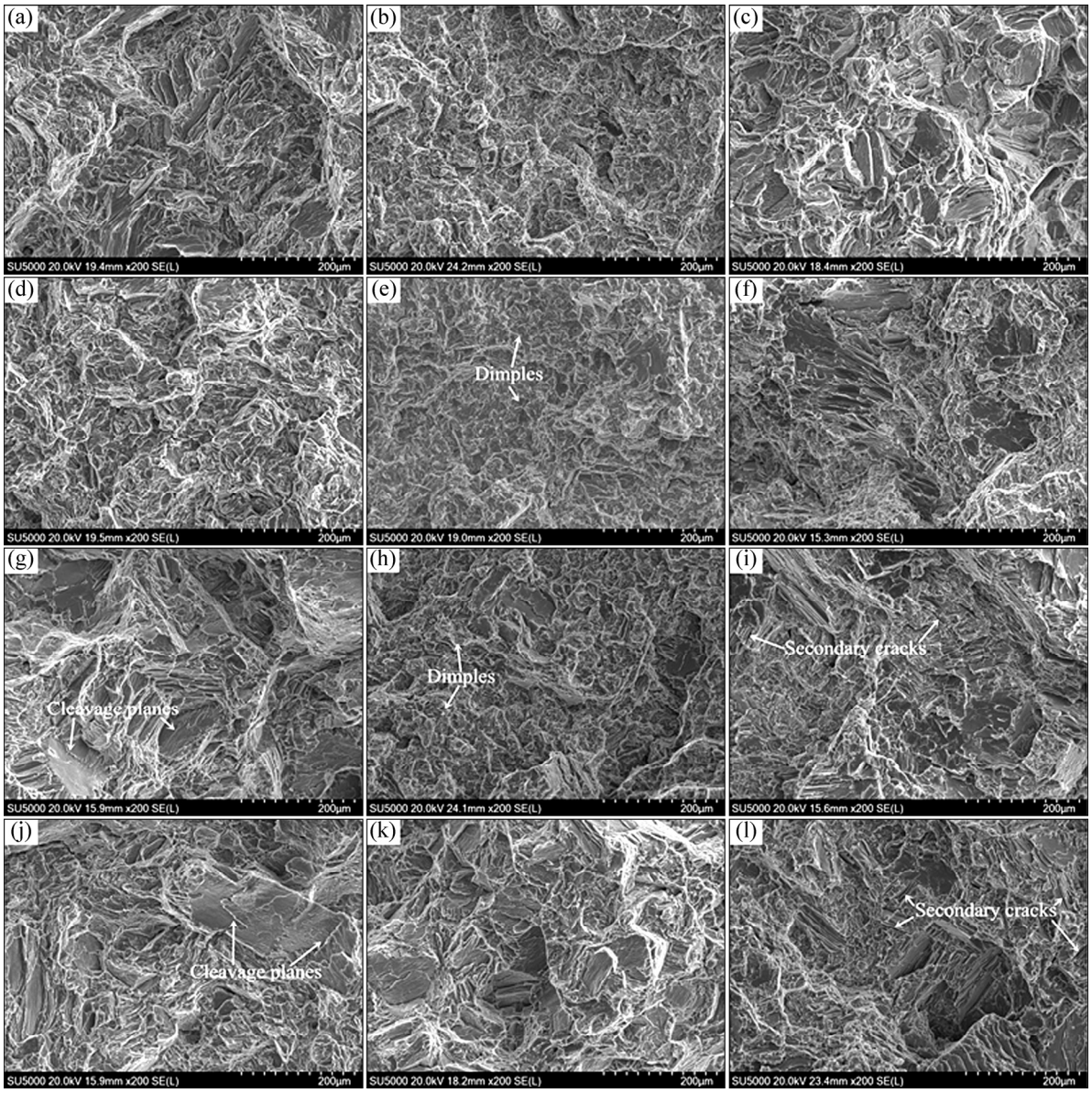

Fig. 14 SEM images of tensile fracture surface of as-cast (a, d, g, j), solution-treated (b, e, h, k) and peak-aged (c, f, i, l) alloys: (a, b, c) Alloy A; (d, e, f) Alloy B; (g, h, i) Alloy C; (j, k, l) Alloy D

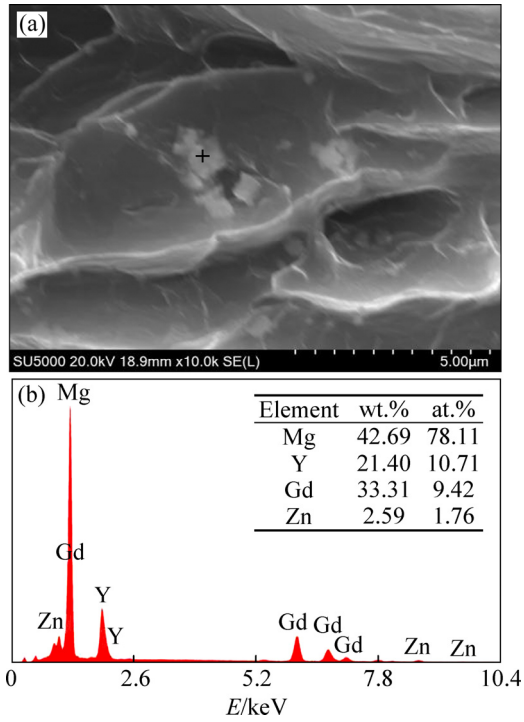

Fig. 15 Magnified SEM image and EDS analysis result of tensile fracture surface of peak-aged alloy B

4 Discussion

The as-cast alloy A is composed of α-Mg and $Mg_{24}(Gd,Y)_5$, while the second phases in the alloy B are $Mg_{24}(Gd,Y,Zn)_5$ and $(Mg,Zn)_3(Gd,Y)$ phases. The $(Mg,Zn)_3(Gd,Y)$ and $Mg_{12}(Gd,Y)Zn$ second phases are observed in the alloys C and D. Moreover, the needle-like phases in the alloys C and D are proven to be stacking faults rather than LPSO phases, and the 18R LPSO phases are noticed only in the alloy D. It can be summed up that there is a transformation in the four as-cast alloys following the order of $Mg_{24}(Gd,Y)_5 \rightarrow Mg_{24}(Gd,Y,Zn)_5 + (Mg,Zn)_3(Gd,Y) \rightarrow (Mg,Zn)_3(Gd,Y)+ Mg_{12}(Gd,Y)Zn$ + stacking faults $\rightarrow$ $(Mg,Zn)_3(Gd,Y)$ + $Mg_{12}(Gd,Y)Zn$ + stacking faults + 18R LPSO with the increase of Zn content. It has been reported that the simultaneous additions of Y and Zn elements can decrease the stacking fault energy, and effectively promote the formation of stacking faults [16,17]. In addition, the stacking faults are first formed in the alloy with 1 wt.% Zn content, whereas 2 wt.% Zn content leads to the formation of stacking faults as well as 18R LPSO phases. The stacking fault can cause weak extra streaks or spots in SEAD patterns, which is similar to 10H, 14H and 18R LPSO phases [18,23,24]. It is indicated that the formation of LPSO phases is related to not only stacking sequence ordered but also chemical composition ordered.

After solution treatment, the $Mg_{24}(Gd,Y)_5$ eutectic compounds in the alloy A have been fully dissolved, and only some small cuboid phases and grain boundaries can be observed. The stacking faults, $Mg_{24}(Gd,Y,Zn)_5$, $(Mg,Zn)_3(Gd,Y)$ and 18R LPSO phases in as-cast Mg−Gd−Y−Zn−Zr alloys are transformed into 14H LPSO phases, which is consistent with reports [25−27]. The 14H LPSO phase is a high temperature stable phase, obtained after 520 °C, 8 h solution treatment, which can significantly prevent the movement of dislocations and growth of grain boundaries, and the grain size decreases from 134.3 to 46.5 μm with the increase of 14H LPSO phase from 0% to 31.9%. It is noteworthy that the addition of 0.5 wt.% Zn can dramatically lead to the formation of 3.4% volume bulk 14H LPSO phases. Several lamellar 14H LPSO phases possessing different orientations in different grains are found to grow parallel with one another from the grain boundaries to the grain interior in the solution-treated alloy C, which suggests that the lamellar LPSO phases have specific orientation relationship with the α-Mg matrix crystals. The bulk 14H LPSO phases mainly distribute at grain boundaries, while the lamellar 14H LPSO phases are often precipitated in the α-Mg matrix and close to the grain boundaries. HUANG et al [28] reported that the morphologies of two 14H LPSO phases change dynamically under different solution treated conditions, and the lamellar 14H LPSO phase precipitates in the grain interior when the solution treatment temperature is above 350 °C.

The variation of the mechanical properties with Zn content must be related to the evolution of the microstructures discussed above. The strengthening mechanisms for cast Mg−RE(−Zn)−Zr alloys in different conditions may typically be divided into: second phase strengthening, solid solution strengthening, grain boundary strengthening and precipitation strengthening [29−31]. The hollow-out skeleton-shaped $(Mg,Zn)_3(Gd,Y)$ phase acts as the main second phase strengthening in the as-cast alloys. XU et al [32] reported that the $(Mg,Zn)_3RE$ phase with a finer net-shape can improve the strength, but the severely coarsened net-shaped $(Mg,Zn)_3RE$ phases are more sensitive to the stress concentration. Namely, the present result is consistent with these investigations. The alloy B shows the optimal mechanical properties in the as-cast condition.

The mechanical properties of these alloys are improved after solution treatment, especially elongation, even if the grain size increases obviously. The solution-treated alloy A has the largest grain size, so only solid solution strengthening contributes to the mechanical properties. The RE elements are dissolved in the α-Mg matrix, and the grains are strengthened by solid atoms, resulting in more cracking resistance to the grains [33].

The alloy C exhibits optimum mechanical properties in the solution treated condition, and the values of UTS, YS and elongation are 253 MPa, 168 MPa and 18.2%, respectively. Its good performances, especially ductility, are attributed to the second phase strengthening of 14H LPSO phase and solid solution strengthening. The RE elements can easily combine with Zn to form the LPSO phase in the Mg−RE−Zn−Zr alloys, which leads to the decrease of RE elements dissolved into the matrix, and the effect of solid solution strengthening is greatly reduced. The 14H LPSO phase has higher elastic moduli and Vickers hardness, which can significantly prevent the movement of dislocations and improve the mechanical properties of Mg−RE−Zn−Zr alloys [7,13,28]. Therefore, the strengthening effect of 14H LPSO phases in the solution-treated alloys is superior to the other strengthening mechanisms, especially for the enhancement of ductility. In addition, the lamellar 14H LPSO phases have a significantly smaller average size than the block-shaped LPSO phases, which can improve the mechanical properties of the alloy C more effectively [28]. However, the coarse LPSO phases lead to a decrease in mechanical properties, such as the alloy D in solution-treated condition.

From Fig. 10, it can be suggested that the aging responses of these alloys decrease with increasing Zn addition. The reason for this is that the content of RE in the supersaturated matrix decreases with increasing Zn addition, and the precipitation of β' phases decreases accordingly, as shown in Fig. 11. There is a competitive demand for RE atoms between the formation of 14H LPSO phase and β' precipitates. The ellipsoidal-shaped β' phases exhibit a semicoherent structure with α-Mg, which can effectively inhibit the slipping of the base plane [22]. These precipitates can reduce the spacing between the particles and effectively enhance the dispersion strengthening. The tensile strength of the solution-treated alloys A, B and C are greatly improved by the precipitation strengthening of β' phases. In the peak-aged alloy A, only precipitation strengthening contributes to the mechanical properties, and the UTY and YS are increased by 106 and 46 MPa, respectively. However, the β' precipitates are coherent with matrix, which may produce precipitates shearing mechanism, leading to an inhomogeneous distribution of slip and reducing the elongation [34]. It is suggested that the β' phases are good to tensile strength while bad to plasticity. ZHENG et al [35] reported that the β' precipitates and LPSO phases can form an intercalated structure, and the spatial interaction between β' and LPSO can hinder the coarsening of both β' and LPSO phases. Both the suitable volume fraction of 14H LPSO phases and the fine ellipsoidal-shaped β' phases make the peak-aged alloy with 0.5 wt.% Zn exhibit excellent comprehensive mechanical properties and the UTS, YS and elongation are 338 MPa, 201 MPa and 6.8%, respectively.

5 Conclusions

(1) The microstructures of the as-cast alloy without Zn consists of α-Mg and $Mg_{24}(Gd,Y)_5$ phases. The alloy with 0.5 wt.% Zn is mainly composed of α-Mg, $Mg_{24}(Gd,Y,Zn)_5$ and $(Mg,Zn)_3(Gd,Y)$ phases. With the addition of Zn increasing to 1 wt.%, the $Mg_{24}(Gd,Y,Zn)_5$ phase disappears and some needle-like stacking faults distribute along the grain boundaries. The 18R LPSO phase is observed in the as-cast alloy with 2 wt.% Zn.

(2) The $Mg_{24}(Gd,Y)_5$ phases are completely dissolved, and the $Mg_{24}(Gd,Y,Zn)_5$, $(Mg,Zn)_3(Gd,Y)$, needle-like stacking faults and 18R LPSO phases all transform into the 14H LPSO phases during solution treatment. With increasing content of Zn to 0.5, 1 and 2 wt.%, the grain size and the number density of the cuboid-shaped phases decrease, and the volume fraction of the 14H LPSO phases increases from 0% to 3.4%, 16.5% and 31.9%.

(3) The ductility of the solution-treated alloys is improved significantly compared with that of as-cast alloys. The solution-treated alloy with 1 wt.% Zn containing several lamellar 14H LPSO phases shows the optimal mechanical properties, and the UTS, YS and elongation are 253 MPa, 168 MPa and 18.2%, respectively.

(4) The density of ellipsoidal-shaped β' phase decreases obviously with increasing Zn content, and the average size of this phase is significantly increased. Both the suitable volume fraction of 14H LPSO phases and the fine ellipsoidal-shaped β' phases make the peak-aged alloy with 0.5 wt.% Zn exhibit excellent comprehensive mechanical properties and the UTS, YS and elongation are 338 MPa, 201 MPa and 6.8%, respectively.

References

[1] LIU K, SUN C C, WANG Z H, LI S B, WANG Q F, DU W B. Microstructure, texture and mechanical properties of Mg−Zn−Er alloys containing *I*-phase and *W*-phase simultaneously [J]. Journal of Alloys and Compounds, 2016, 665: 76−85.

[2] ZHU S Z, LUO T J, YANG Y S. Improving mechanical properties of age-hardenable Mg−6Zn−4Al−1Sn alloy processed by double-aging treatment [J]. Journal of Materials Science & Technology, 2017, 33: 1249−1254.

[3] LIU Hong-hui, NING Zhi-liang, YI Jun-ying, MA Qian, SUN Hai-chao, HUANG Yong-jiang, SUN Jian-fei. Effect of Dy addition on microstructure and mechanical properties of Mg−4Y−3Nd−0.4Zr alloy [J]. Transactions of Nonferrous Metals Society of China, 2017, 27(4): 797−803.

[4] LU R P, WANG J F, CHEN Y L, QIN D Z, YANG W X, WU Z S. Effects of heat treatment on the morphology of long-period stacking

ordered phase, the corresponding damping capacities and mechanical properties of Mg−Zn−Y alloys [J]. Journal of Alloys and Compounds, 2015, 639: 541−546.

[5] CAO Liang, LIU Wen-cai, LI Zhong-quan, WU Guo-hua, XIAO Lu, WANG Shao-hua, DING Wen-jiang. Effect of heat treatment on microstructures and mechanical properties of sand-cast Mg−10Gd−3Y−0.5Zr magensium alloy [J]. Transactions of Nonferrous Metals Society of China, 2014, 24(3): 611−618.

[6] XU C, ZHENG M Y, XU S W. Ultra high-strength Mg−Gd−Y−Zn−Zr alloy sheets processed by large-strain hot rolling and ageing [J]. Materials Science and Engineering A, 2012, 547: 93−98.

[7] WANG J F, SONG P F, HUANG S, PAN F S. High-strength and good-ductility Mg−RE−Zn−Mn magnesium alloy with long-period stacking ordered phase [J]. Materials Letters, 2013, 93: 415−418.

[8] LUO Z P, ZHANG S Q. High-resolution electron microscopy on the *X*-$Mg_{12}ZnY$ phase in a high strength Mg−Zn−Zr−Y magnesium alloy [J]. Journal of Materials Science Letters, 2000, 19: 813−815.

[9] RONG W, ZHANG Y, WU Y, SUN M, CHEN J, WANG Y, HAN J, PENG L, DING H. Effects of Zr and Mn additions on formation of LPSO structure and dynamic recrystallization behavior of Mg−15Gd−1Zn alloy [J]. Journal of Alloys and Compounds, 2017, 692: 805−816.

[10] LI D, ZHANG J, QUE Z, XU C, NIU X. Effects of Mn on the microstructure and mechanical properties of long period stacking ordered Mg95Zn2.5Y2.5 alloy [J]. Materials Letters, 2013, 109: 46−50.

[11] YIN J, LU C, MA X, DAI B, CHEN H. Investigation of two-phase Mg−Gd−Ni alloys with highly stable long period stacking ordered phases [J]. Intermetallics, 2016, 68: 63−70.

[12] MATSUDA M, LI S, KAWAMURA Y. Variation of long-period stacking order structures in rapidly solidified Mg97Zn1Y2 alloy [J]. Materials Science and Engineering A, 2005, 393: 269−274.

[13] CHINO Y, MABUCHI M, HAGIWARA S, IWASAKI H, YAMAMOTO A, TSUBAKINO H. Novel equilibrium two phase Mg alloy with the long-period ordered structure [J]. Scripta Materialia, 2004, 51: 711−714.

[14] NISHIDA M, KAWAMURA Y, YAMAMURO T. Formation process of unique microstructure in rapidly solidified Mg97Zn1Y2 alloy [J]. Materials Science and Engineering A, 2004, 375−377: 1217−1223.

[15] KAWAMURA Y, HAYASHI K, INOUE A, MASUMOTO T. Rapidly solidified powder metallurgy $Mg_{97}Zn_1Y_2$ alloys with excellent tensile yield strength above 600 MPa [J]. Materials Transactions, 2001, 42: 1171−1174.

[16] SUZUKI M, KIMURA T, KOIKE J, MARUYAMA K. Effects of zinc on creep strength and deformation substructures in Mg−Y alloy [J]. Materials Science and Engineering A, 2004, 387−389: 706−709.

[17] SUZUKI M, KIMURA T, KOIKE J, MARUYAMA K. Strengthening effect of Zn in heat resistant Mg−Y−Zn solid solution alloys [J]. Scripta Materialia, 2003, 48: 997−1002.

[18] ZHU Y M, MORTON A J, NIE J F. The 18R and 14H long-period stacking ordered structures in Mg−Y−Zn alloys [J]. Acta Materialia, 2010, 58: 2936−2947.

[19] LIU H, BAI J, YAN K, YAN J L, MA A B, JIANG J H. Comparative studies on evolution behaviors of 14H LPSO precipitates in as-cast and as-extruded Mg−Y−Zn alloys during annealing at 773 K [J]. Materials and Design, 2016, 93: 9−18.

[20] LI Y L, WU G H, CHEN A T, NODOOSHAN H R J, LIU W C, WANG Y X, DING W J. Effects of Gd and Zr additions on the microstructures and high-temperature mechanical behavior of Mg−Gd−Y−Zr magnesium alloys in the product form of a large structural casting [J]. Journal of Materials Research, 2015, 30: 3461−3473.

[21] ZHENG K Y, DONG J, ZENG X Q, DING W J. Precipitation and its effect on the mechanical properties of a cast Mg−Gd−Nd−Zr alloy [J]. Materials Science and Engineering A, 2008, 489: 44−54.

[22] HAN X Z, XU W C, SHAN D B. Effect of precipitates on microstructures and properties of forged Mg−10Gd−2Y−0.5Zn−0.3Zr alloy during ageing process [J]. Journal of Alloys and Compounds, 2011, 509: 8625−8631.

[23] EGUSA D, ABE E. The structure of long period stacking/order Mg−Zn−RE phases with extended non-stoichiometry ranges [J]. Acta Materialia, 2012, 60: 166−178.

[24] YAMASAKI M, MATSUSHITA M, HAGIHARA K, IZUNO H, ABE E, KAWAMURA Y. Highly ordered 10H-type long-period stacking order phase in a Mg−Zn−Y ternary alloy [J]. Scripta Materialia, 2014, 78−79: 13−16.

[25] CHENG P, ZHAO Y H, LU R P, HOU H, BU Z Q, YAN F. Effect of Ti addition on the microstructure and mechanical properties of cast Mg−Gd−Y−Zn alloys [J]. Materials Science and Engineering A, 2017, 708: 482−491.

[26] YAMASAKI M, NISHIJIMA M, SASAKI M, HIRAGA K, KAWAMURA Y. Formation of 14H long period stacking ordered structure and profuse stacking faults in Mg−Zn−Gd alloys during isothermal aging at high temperature [J]. Acta Materialia, 2007, 55: 6798−6805.

[27] XU C, ZHENG M Y, WU K, WANG E D, FAN G H, XU S W, KAMADO S, LIU X D, WANG G J, LV X Y. Effect of cooling rate on the microstructure evolution and mechanical properties of homogenized Mg−Gd−Y−Zn−Zr alloy [J]. Materials Science and Engineering A, 2013, 559: 364−370.

[28] HUANG S, WANG J F, HOU F, HUANG X H, PAN F S. Effect of Gd and Y contents on the microstructural evolution of long period stacking ordered phase and the corresponding mechanical properties in Mg−Gd−Y−Zn−Mn alloys [J]. Materials Science and Engineering A, 2014, 612: 363−370.

[29] LUTJERING G, ALBRECHT J, SAUER C, KRULL T. The influence of soft, precipitate-free zones at grain boundaries in Ti and Al alloys on their fatigue and fracture behavior [J]. Materials Science and Engineering A, 2007, 468−470: 201−209.

[30] GAO L, CHEN R E, HAN E H. Microstructure and strengthening mechanisms of a cast Mg−1.48Gd−1.13Y−0.16Zr (at.%) alloy [J]. Journal of Materials Science, 2009, 44: 4443−4454.

[31] HE S M, ZENG X Q, PENG L M, GAO X, NIE J F, DING W J. Microstructure and strengthening mechanism of high strength Mg−10Gd−2Y−0.5Zr alloy [J]. Journal of Alloys and Compounds, 2007, 427: 316−323.

[32] XU D K, TANG W N, LIU L, XU Y B, HAN E H. Effect of W-phase on the mechanical properties of as-cast Mg−Zn−Y−Zr alloys [J]. Journal of Alloys and Compounds, 2008, 461: 248−252.

[33] FU P H, PENG L M, JIANG H Y, CHANG J W, ZHAI C Q. Effects of heat treatments on the microstructures and mechanical properties of Mg−3Nd−0.2Zn−0.4Zr (wt.%) alloy [J]. Materials Science and Engineering A, 2008, 486: 183−192.

[34] SUNDARARAMAN M, MUKHOPADHYAY P, BANERJEE S. Deformation behaviour of γ'' strengthened Inconel 718 [J]. Acta Materialia, 1988, 36: 847−864.

[35] ZHENG J X, CHEN B. Interactions between long-period stacking ordered phase and β' precipitate in Mg−Gd−Y−Zn−Zr alloy: Atomic-scale insights from HAADF-STEM [J]. Materials Letters, 2016, 176: 223−227.

Zn 添加对铸造 Mg−Gd−Y−Zr 合金组织和力学性能的影响

丁志兵[1,2]，赵宇宏[1]，鲁若鹏[1]，原梅妮[2]，王志军[2]，李会军[3]，侯 华[1]

1. 中北大学 材料科学与工程学院，太原 030051；
2. 中北大学 机电工程学院，太原 030051；
3. School of Mechanical, Materials and Mechatronic Engineering,
University of Wollongong, Wollongong, NSW 2522, Australia

摘 要：研究 Zn 添加对 Mg−10Gd−3Y−0.6Zr(wt.%)合金在铸态、固溶态和峰时效态下显微组织和力学性能的影响。实验结果表明，不含 Zn 的铸态合金由 α-Mg 和 $Mg_{24}(Gd,Y)_5$ 相组成，而含 0.5 wt.% Zn 的铸态合金由 α-Mg、$(Mg,Zn)_3(Gd,Y)$和 $Mg_{24}(Gd,Y,Zn)_5$ 相组成。随着 Zn 含量增加到 1 wt.%，$Mg_{24}(Gd,Y,Zn)_5$ 相消失，一些针状堆垛层错沿晶界分布。此外，在含 2 wt.% Zn 的铸态合金中观察到 18R 型长周期结构相。固溶处理后，$Mg_{24}(Gd,Y)_5$ 和 $Mg_{24}(Gd,Y,Zn)_5$ 共晶相完全溶解，$(Mg,Zn)_3(Gd,Y)$相、针状堆垛层错和 18R 型长周期结构相均转化为 14H 型长周期结构相。适当体积分数的 14H 型长周期结构相和细小的椭球状 β'相共同赋予峰时效态下含 0.5 wt.% Zn 合金优良的综合力学性能，该合金的抗拉强度、屈服强度和伸长率分别为 338 MPa、201 MPa 和 6.8%。

关键词：镁合金；热处理；显微组织；力学性能；长周期结构相

(Edited by Bing YANG)